Received: 24 April 2024 | Accepted: 6 May 2024

DOI: 10.1096/fba.2024-00047

RESEARCH ARTICLE

FASEB BioAdvances WILEY

Heterogeneous distribution of mitochondria and succinate dehydrogenase activity in human airway smooth muscle cells

Sanjana Mahadev Bhat | **Gary C. Sieck**

Department of Physiology and Biomedical Engineering, Mayo Clinic, Rochester, Minnesota, USA

Correspondence
Gary C. Sieck, Department of Physiology and Biomedical Engineering, Mayo Clinic, 200 First Street SW, Rochester, MN 55905, USA.
Email: sieck.gary@mayo.edu

Abstract

Succinate dehydrogenase (SDH) is a key mitochondrial enzyme involved in the tricarboxylic acid cycle, where it facilitates the oxidation of succinate to fumarate, and is coupled to the reduction of ubiquinone in the electron transport chain as Complex II. Previously, we developed a confocal-based quantitative histochemical technique to determine the maximum velocity of the SDH reaction (SDH_{max}) in single cells and observed that SDH_{max} corresponds with mitochondrial volume density. In addition, mitochondrial volume and motility varied within different compartments of human airway smooth muscle (hASM) cells. Therefore, we hypothesize that the SDH activity varies relative to the intracellular mitochondrial volume within hASM cells. Using 3D confocal imaging of labeled mitochondria and a concentric shell method for analysis, we quantified mitochondrial volume density, mitochondrial complexity index, and SDH_{max} relative to the distance from the nuclear membrane. The mitochondria within individual hASM cells were more filamentous in the immediate perinuclear region and were more fragmented in the distal parts of the cell. Within each shell, SDH_{max} also corresponded to mitochondrial volume density, where both peaked in the perinuclear region and decreased in more distal parts of the cell. Additionally, when normalized to mitochondrial volume, SDH_{max} was lower in the perinuclear region when compared to the distal parts of the cell. In summary, our results demonstrate that SDH_{max} measures differences in SDH activity within different cellular compartments. Importantly, our data indicate that mitochondria within individual cells are morphologically heterogeneous, and their distribution varies substantially within different cellular compartments, with distinct functional properties.

Abbreviations: α-SMA, α-smooth muscle actin; ETC, electron transport chain; GL, gray level; hASM, human airway smooth muscle; IMM, inner mitochondrial membrane; MCI, mitochondrial complexity index; mPMS, 1-methoxy-5-methylphenazinium methyl sulfate; NBT, nitro blue tetrazolium; NBT_{dfz}, nitro blue tetrazolium diformazan; OD, optical density; OCR, oxygen consumption rate; ROS, reactive oxygen species; SDH, succinate dehydrogenase; TCA, tricarboxylic acid cycle; TEMPOL, 4-hydroxy-2,2,6,6-tetramethylpiperidine-1-oxyl.

KEYWORDS
airway smooth muscle, confocal microscope, intracellular distribution, mitochondria, succinate dehydrogenase

1 | INTRODUCTION

Succinate dehydrogenase (SDH) is an enzyme present in the inner mitochondrial membrane (IMM) that plays a critical role in cellular respiration. SDH is a key enzyme of the tricarboxylic acid (TCA) cycle and Complex II of the electron transport chain (ETC).[1] In the TCA cycle, SDH catalyzes the oxidation of succinate to fumarate and feeds electrons to the ETC, thereby linking the TCA cycle and the ETC. In the ETC, SDH accepts electrons from succinate and transfers them to FAD, thereby reducing it to $FADH_2$. The electrons are then transferred to ubiquinone (coenzyme Q), which subsequently contributes to the generation of the proton gradient and the synthesis of ATP by ATP synthase (Figure 1A).[2–4]

The maximum velocity of the SDH reaction (SDH_{max}) can be measured *in situ* using a quantitative histochemical technique (Figure 1B).[5-8] The use of this technique was validated in skeletal muscle fibers and more recently in single human airway smooth muscle (hASM) cells.[9-13] Previously, we found that SDH_{max} corresponds with mitochondrial volume density within a cell.[12] However, when SDH_{max} is normalized for mitochondrial volume, SDH activity appears to vary depending on mitochondrial morphometry, where SDH_{max} is lower in cells in which mitochondria are more fragmented. Provided ETC complexes are embedded within the IMM, changes in mitochondrial inner membrane topology can influence mitochondrial bioenergetic processes.[14,15] Since SDH is localized on the IMM, the decrease in SDH_{max} is consistent with more fragmented mitochondria having lower IMM surface area.

Previously in hASM cells, we observed that mitochondria are primarily distributed immediately around the nucleus, with most mitochondrial volume localized in the perinuclear region (within 10–20 μm of the nuclear membrane).[16] In addition, there are differences in mitochondrial morphology and motility between the perinuclear and distal compartments of hASM cells.[16-18] Perinuclear mitochondria in hASM cells are visibly more filamentous and more mobile than mitochondria in more distal regions.[18] In general, cells with more motile mitochondria display increased mitochondrial oxygen consumption rate.

By using the *in situ* assay of SDH_{max} and a non-disruptive labeling of mitochondria, the goal of the present study was to explore the relationship between SDH_{max} and the distribution and morphometry of mitochondria in the perinuclear and distal compartments of hASM cells. We hypothesize that SDH_{max} and mitochondrial

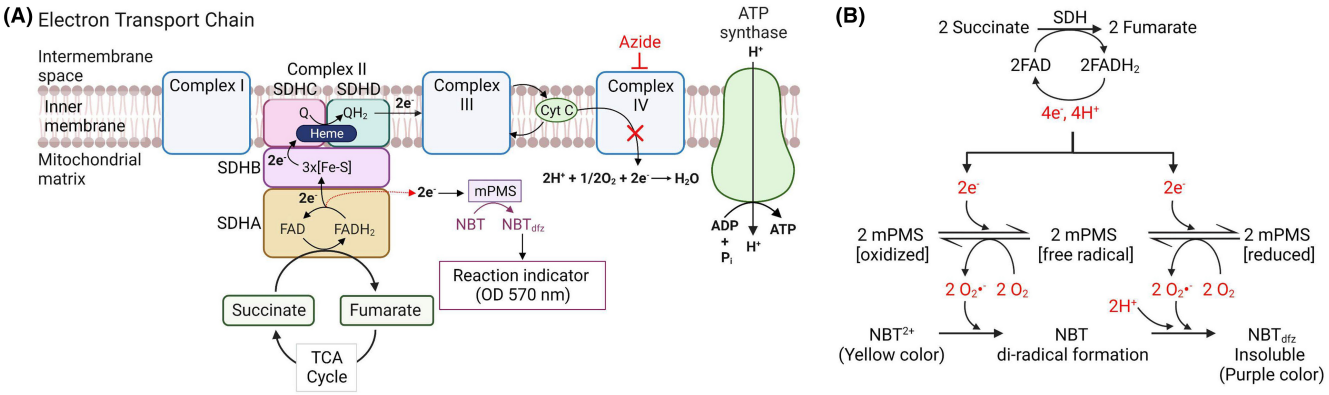

FIGURE 1 Overview of the SDH assay. (A) An overview of the quantitative histochemical technique to measure the maximum velocity of the succinate dehydrogenase reaction (SDH_{max}). The schematic representation depicts the transfer of electrons (e^-) from the oxidation of succinate to fumarate in the TCA cycle into the ETC concluding at the terminal electron acceptor, complex IV. The SDH reaction is performed in the presence of azide to inhibit cytochrome oxidase (Complex IV) and an exogenous electron carrier, mPMS. As the terminal electron acceptor, mPMS promotes the progressive reduction of NBT to its diformazan (NBT_{dfz}) which is used as the reaction indicator. The accumulation of NBT_{dfz} within individual hASM cells is measured as the change in OD at 570 nm. (B) Schematic representation demonstrating the electron transport leading to the reduction of NBT, in the SDH assay. With succinate as substrate, the transfer of electrons from $FADH_2$ to NBT is proposed along the classical pathway starting at complex II (Created with BioRender.com). hASM, human airway smooth muscle; NBT, nitroblue tetrazolium; OD, optical density; SDH, succinate dehydrogenase; TCA, tricarboxylic acid; ETC, electron transport chain.

volume density are higher in the perinuclear compared to the distal compartments of hASM cells. We also hypothesize that SDH_{max} is higher in the perinuclear compartment reflecting the more filamentous morphometry of mitochondria in the perinuclear compartment.

2 | MATERIALS AND METHODS

2.1 | Anonymous patient selection

The study was reviewed by Mayo Clinic's Institutional Review Board (IRB #16-009655) and considered to be of minimal risk and therefore exempt from further review for the following reasons. All potential patients were consented before surgery in a non-threatening environment. Written informed consent was obtained from patients during presurgical evaluation (in the Pulmonary, Oncology, or Thoracic Surgery Clinics). Patient history was provided at the time of tissue acquisition for the recording of sex, demographics, pulmonary disease status, pulmonary function testing, imaging, co-morbidities, and medications, but no patient identifiers were stored. Accordingly, samples were numbered, but patient identifiers were never stored or attached to the samples, preventing retrospective patient identification from samples alone. From a larger set of patient donors (ranging in age from 30 to 80 years), a total of six (3 female and 3 male) patients were selected for this study after the exclusion of patients with chronic lung disease, asthma, any other respiratory diseases, and any recent history of smoking (Table 1). During surgery, bronchiolar tissue samples containing third to sixth-generation bronchi were obtained and evaluated by clinical pathology. From all bronchiolar tissue samples, only normal regions of the tissue were included.

2.2 | Dissociation of cells from bronchiolar tissue

From the bronchiolar tissue, the smooth muscle layer was dissected, and cells were dissociated by enzymatic digestion using papain and collagenase with ovomucoid/albumin separation as per the manufacturer's instructions (Worthington Biochemical, Lakewood, NJ) and as previously described.[17,19,20] Cells were maintained at 37°C (5% CO_2—95% air, pH 7.4) in phenol red-free DMEM/F-12 medium (Invitrogen, Carlsbad, CA) supplemented with 10% fetal bovine serum (FBS) and 100 U/mL of penicillin/streptomycin. To ensure the use of cells within their optimal phenotypic and metabolic characteristics, cells were only cultured for 1–3 passages. Before experiments, the cells were serum-deprived for 48 h by replacing the growth medium with DMEM/F-12 medium lacking serum. The dissociated bronchiolar cells were phenotyped prior to experimental use.

TABLE 1 hASM patient demographic profile.

Patient	Sex	Age (years)	Respiratory disease	Smoking status
1	F	41	None	Past-Smoker
2	M	80	None	Non-Smoker
3	F	80	None	Non-Smoker
4	M	56	None	Non-Smoker
5	F	78	None	Past-Smoker
6	M	78	None	Non-Smoker

2.3 | Immunocytochemical labeling and phenotyping dissociated hASM cells

The hASM phenotype of isolated cells was confirmed by immunocytochemical analysis of α-smooth muscle actin (α-SMA) expression as previously described.[12,18,21-24] Briefly, dissociated cells were plated at a density of ~10,000 cells/well in a Nunc™ Lab-Tek™ II Chamber 8-well multichamber slide (Thermo Fisher Scientific, Rockford, IL), incubated till cell adherence was achieved and serum-deprived. Cells were fixed with 4% paraformaldehyde in 1X phosphate-buffered saline (PBS) for 10 min at room temperature and washed with 1X PBS. To prevent non-specific antibody binding, cells were incubated for 1 h at room temperature in a blocking buffer containing 10% normal donkey serum (Sigma-Aldrich, St. Louis, MO), 0.2% triton X-100 and 1X PBS. Cells were then incubated overnight at 4°C with anti-α-SMA antibody (1:500 dilution, rabbit polyclonal; Abcam Cat# ab5694, RRID:AB_2223021; Boston, MA) in a diluent solution (2.5% normal donkey serum, 0.25% sodium azide, 0.2% triton X-100, 1X PBS). Following this, the cells were incubated for 1 h at room temperature in donkey anti-rabbit biotin-conjugated secondary antibody (1:400, diluted in antibody diluent; Jackson ImmunoResearch Labs Cat# 711-067-003, RRID:AB_2340595; West Grove, PA), followed by Streptavidin Alexa Fluor 568 (1:200 in PBS; Thermo Fisher Scientific Cat# S-11226, RRID:AB_2315774; Carlsbad, CA) for 30 min at room temperature. The cells were mounted using Fluoro-Gel II mounting medium with 4′,6-Diamidino-2-Phenylindole, Dihydrochloride (DAPI; Electron Microscopy Sciences, Hatfield, PA). Dissociated cells were imaged to distinguish α-SMA expressing hASM cells using a Nikon ECLIPSE Ti inverted microscope system (RRID:SCR_021242) with a ×60/1.4 NA oil-immersion objective and the percentage of hASM cells was determined as a fraction of the total dissociated cells (determined from DAPI labeled nuclei; Figure 2).

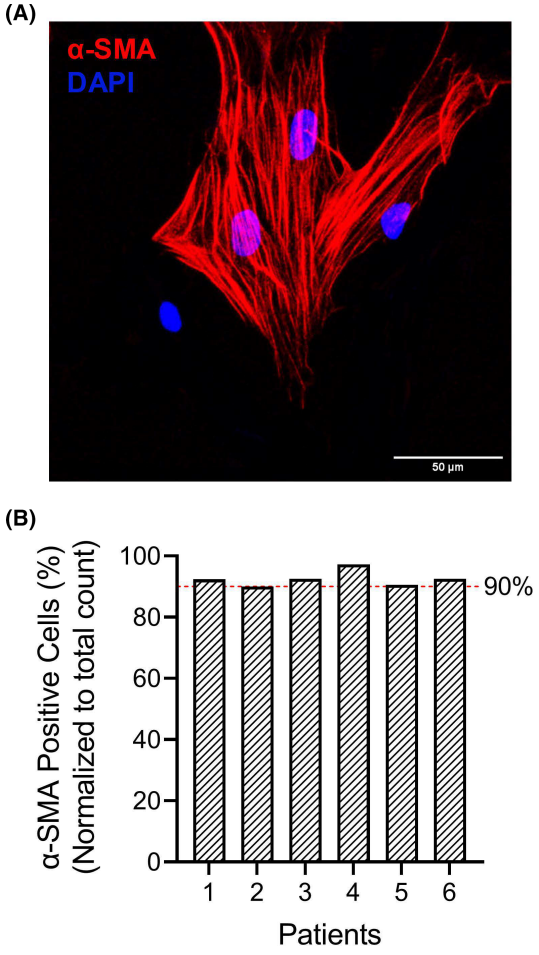

FIGURE 2 Confirmation of hASM phenotype. (A) Representative maximum intensity Z projection image of dissociated cells show the phenotype of dissociated hASM cells based on their immunoreactivity to α-SMA expression and larger size (scale bar = 50 µm). (B) Column bar graph represents the percentage of hASM cells present in dissociated cells determined by the fraction of α-SMA expressing cells to total number of cells (determined from DAPI) from six patient samples ($n = 120$ hASM cells per patient). Note that ≥90% of total dissociated cells were immunoreactive to α-SMA. hASM, human airway smooth muscle; SMA, smooth muscle actin.

2.4 | Quantitative histochemical measurement of SDH reaction

For the quantitative histochemical procedure, images were acquired using a Nikon A1R Confocal Laser Scanning Microscope (RRID:SCR_020317) with a ×60/1.4 NA oil-immersion objective at 12-bit resolution into a 1024 × 1024-pixel array using the transmitted light channel. An interference filter with a peak emission wavelength of 570 nm was placed in the path of light to limit the spectral range of the light source to the maximum absorption wavelength of nitroblue tetrazolium diformazan (NBT_{dfz}). The measured gray level (GL) of the microscope was calibrated to known optical density (OD) units using a photographic density step-wedge tablet (0.04–2.20 OD units in increments of 0.15 OD; Stouffer Industries, Mishawaka, IN), as previously described.[12] The dynamic range of the microscope was adjusted to take advantage of the full range of OD while avoiding saturation of the images at both ends of the OD range, as described previously.[12]

The quantitative histochemical procedure for measuring SDH_{max} was performed in hASM cells, which has been previously described in detail.[5-8,12,25-35] The hASM cells were plated in 8-well Ibidi µ-slide plates (Ibidi GmbH, Gewerbehof Gräfelfing, Germany) at a density of ~15,000 cells/well and incubated to allow for cell adherence, followed by serum deprivation. Briefly, hASM cells were exposed to solutions containing either 80 mM succinate (substrate) or no succinate (without substrate). Both solutions also contained: 1.5 mM nitroblue tetrazolium (NBT; reaction indicator), 5 mM ethylenediaminetetraacetic acid (EDTA), 1 mM 1-methoxy-5-methylphenazinium methyl sulfate (mPMS; exogenous electron carrier), and 0.75 mM sodium azide (Complex IV inhibitor) in 0.1 M phosphate buffer (pH: 7.6). In previous studies, we determined that the SDH enzymatic reaction is not substrate limited at succinate concentrations of 80 mM.[6,7,9,11-13] In a separate series of experiments, the dependency of the SDH reaction on succinate concentration was reassessed, and a concentration of 80 mM was found to produce SDH_{max} in hASM cells.

In the quantitative histochemical procedure, the progressive precipitation and accumulation of NBT_{dfz} due to the reduction of NBT was quantified as change in OD from images acquired every 15 s over an 8-min period (Figure 3A). Previously, we explored the impact of changing path length by changing optical slice thickness and confirmed that path length was controlled by optical slice thickness.[12] Therefore, Z-stacks were acquired every 15 s with optical slice thickness set at 0.5 µm and sampling depth was restricted to 5 µm in the *Z*-axis (2.5 µm above and below the nuclear centroid) and analyzed using NIS-Elements software (version 5.20.02; RRID:SCR_014329; Nikon Instruments Inc., Melville, NY). hASM cells were delineated as the region of interest (ROI), and the nucleus was excluded from the ROI. As the SDH reaction proceeded, the change in OD within the selected 3D ROI was measured every 15 s across the 8-min period. The linearity of the SDH reaction across the 8-min period was confirmed by the change in OD within a delineated hASM cell (Figure 3B; $R^2 = 0.99$). From this, the SDH_{max} was then determined using the Beer–Lambert equation (below):

$$SDH_{max} = \frac{d[NBT_{dfz}]}{dt} = \frac{\frac{dOD}{dt}}{kl} \quad (1)$$

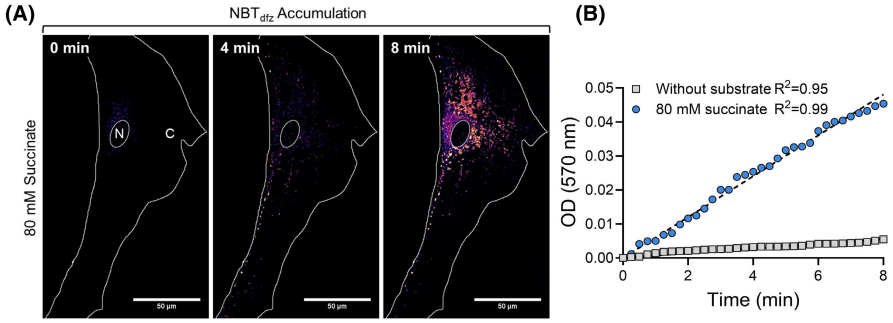

FIGURE 3 SDH reaction is linear over time. (A) Representative images show the change in OD within delineated hASM cell during the SDH reaction at 0, 4, and 8 min. Individual hASM cells were delineated as the region of interest (ROI) for measuring the change in OD while the nucleus was excluded from the ROI (scale bar = 50 µm; N: Nucleus, C: Cytoplasm). To aid in visualizing the NBT_{dfz} accumulation within hASM cells, the original gray-scale images were manually thresholded and the LUTs were inverted to be represented as a heat map using NIS-Elements software. (B) In hASM cells, the OD was measured every 15 s over an 8-min period, with and without succinate (substrate). The SDH reaction was linear ($R^2 = 0.99$) across the 8-min period in the presence of succinate. The rate of SDH reaction in the presence of succinate was significantly higher compared to that without succinate ($R^2 = 0.95$, $p < 0.0001$). Data represent results from one bronchial sample (patient), squares represent SDH reaction performed without succinate, and circles represent SDH reaction performed with succinate. Results were analyzed using a simple linear regression model. Statistical analyses were based on measurements from $n = 10$ cells per patient, from one bronchial sample (patients). NBT, nitroblue tetrazolium diformazan; OD, optical density; SDH, succinate dehydrogenase.

where OD is measured based on the calibrated gray level of NBT_{dfz} accumulation, k is the molar extinction coefficient for NBT_{dfz} (26,478 M^{-1} cm^{-1}), and l is the path length for light absorbance (0.5 µm optical slice thickness). The SDH_{max} within individual hASM cells was expressed as millimoles of fumarate per liter of cell per min.

The temperature at which the SDH assay can be performed optimally was assessed prior to any experiments. SDH_{max} was measured in hASM cells at room temperature (25°C) and physiological temperature (37°C), and the temperature dependency of SDH_{max} was determined as Q_{10}. SDH_{max} measured at 37°C was significantly increased compared to 25°C and had a Q_{10} of 2.97. Inhibition of Complex IV by sodium azide is known to significantly increase the production of reactive oxygen species (ROS) which can cause non-specific reduction of NBT.[36] To circumvent ROS-mediated reduction of NBT, SDH_{max} was measured in hASM cells treated with TEMPOL (4-hydroxy-2,2,6,6-tetra methylpiperidine-1-oxyl), a ROS scavenger. While SDH_{max} remained unchanged at 25°C with and without TEMPOL, at 37°C SDH_{max} in TEMPOL-treated hASM cells significantly decreased compared to SDH_{max} in untreated control cells. Therefore, all SDH_{max} measurements in the present study were performed at room temperature.

In all assays, multiple hASM cells (identified by size and elongated shape) were visualized within a single microscopic field. Based on an *a prior* power analysis of variance in SDH_{max} measurements in untreated hASM cells, $n = 5$ individual hASM cells per group (treated or untreated) per bronchiolar sample (from six patients) were included for analysis.

2.5 | Specificity of the histochemical reaction for SDH

The specificity of the SDH assay was assessed by malonate-mediated inhibition of SDHA or by siRNA-mediated knockdown of SDHB in hASM cells. SDH consists of four subunits, subunits A through D. Here, subunit A (SDHA, a flavoprotein) and subunit B (SDHB, Fe-S protein) together form the catalytic core of the complex,[1,37,38] whereas subunit C (SDHC) and subunit D (SDHD) anchor the complex to the IMM.[1-4,37,38] To inhibit SDHA, hASM cells were treated with malonate, an inhibitor for SDH acting competitively on the carboxylate site (succinate binding site) of SDHA subunit.[39-42] The SDH_{max} was measured at room temperature in hASM cells that were either treated with 1 mM malonate for 24 h (Sigma-Aldrich, St. Louis, MO) or untreated (control).

2.6 | siRNA-mediated knockdown of SDHB subunit

Three custom-designed dicer-substrate small interfering RNAs (DsiRNA; Integrated DNA Technologies Inc., Coralville, IA) targeting SDHB were used to achieve successful knockdown of SDHB subunit. Prior to performing the knockdown, the transfection efficiency was first evaluated using a fluorescently tagged DsiRNA (TYE563). The hASM cells were plated in 8-well Ibidi µ-slide plates (Ibidi GmbH, Gewerbehof Gräfelfing, Germany) at a density of

~15,000 cells/well and incubated to allow for cell adherence. For the transfection, 10 nM of TYE563 siRNA and 10 nM scrambled siRNA (negative control, NC) were diluted in Opti-MEM media and gently mixed with lipofectamine 2000 (2 μg/mL; Invitrogen, Carlsbad, CA) according to the manufacturer's instructions.[43] Following incubation for 20 min at room temperature, the transfection mixture was added onto the cells and the cells were further incubated at 37°C for 24 h. Post-transfection, the hASM cells were mounted using Fluoro-Gel II mounting medium with DAPI (Electron Microscopy Sciences, Hatfield, PA) and imaged using the same inverted microscope system used for immunocytochemical analysis as described above (Figure S1A). Once the transfection efficiency was confirmed, hASM cells with SDHB knockdown were generated. For this, 10 nM SDHB siRNA (R1, R2, and R3) and 10 nM scrambled siRNA (negative control, NC) were diluted in Opti-MEM media and gently mixed with lipofectamine 2000 (2 μg/mL; Invitrogen, Carlsbad, CA) according to the manufacturer's instructions.[43] Following incubation for 20 min at room temperature, the transfection mixture was added onto the cells and the cells were further incubated at 37°C for 24 h. Post-transfection, the percentage knockdown was measured by qPCR and western blot analysis of the target gene and protein, respectively (Figure S1B–G). The sequences of all siRNAs used are listed in Table 2.

2.7 | RNA extraction, cDNA preparation, and qPCR

Total RNA was extracted from SDHB-knockdown and NC hASM cells using RNeasy extraction kit (Qiagen, Hilden, Germany) as per the manufacturer's instruction. In brief, hASM cells were lysed and subjected to ethanol-mediated extraction of RNA. Genomic DNA was removed by an on-column DNase treatment. Extracted RNA samples were quantified using a Thermo Scientific NanoDrop One/One^{C} Microvolume UV–Vis Spectrophotometer (RRID:SCR_023005; Thermo Fisher Scientific, Rockville, IL). A total of 500 ng of RNA was used for complementary DNA (cDNA) synthesis using the high-capacity cDNA reverse transcription kit (Invitrogen, Carlsbad, CA) following the manufacturer's instructions. qPCR was performed using 500 ng of cDNA for the target gene of interest in triplicates using a Roche Light Cycler 480 Instrument (RRID:SCR_020502; Roche, Indianapolis, IN), and the mRNA expression of target genes were analyzed using the $2^{-\Delta\Delta CT}$ method.[44] 40S ribosomal protein S16 (RPS16) was used as the housekeeping gene. No-template negative controls and dissociation curves were run for all reactions to exclude cross-contamination. The primer sequences used for the target genes are listed in Table 3.

2.8 | Protein extraction and western blot

Protein samples were extracted from isolated hASM cells using 1X cell lysis buffer (Cell Signaling Technology, Danvers, MA) supplemented with protease (cOmplete, Protease inhibitor cocktail; Roche, Basel, Switzerland) and phosphatase inhibitors (PhosSTOP; Roche, Basel, Switzerland). The concentration of the extracted protein was measured by DC (detergent compatible) protein assay (Bio-Rad, Hercules, CA) following the manufacturer's instructions. For each western blot, 40 μg of total protein from each sample was denatured at 95°C for 5 min in 1X laemmli sample buffer with 5% β-mercaptoethanol and loaded into 4%–20% Criterion™ TGX Stain-Free™ protein gel (Bio-Rad, Hercules, CA). Once separated, the total protein loaded into each lane was visualized using the Bio-Rad ChemiDoc MP imaging system (RRID:SCR_019037; Hercules, CA). The separated protein bands were then transferred to a polyvinylidene difluoride (PVDF) membrane (0.2 μm; Bio-Rad, Hercules, CA) using the Bio-Rad Trans Blot Turbo system (RRID:SCR_023156; Hercules, CA). Following transfer, the membranes were blocked using EveryBlot blocking buffer (Bio-Rad, Hercules, CA) for 1 h at room temperature, followed by overnight incubation at 4°C in anti-SDHB antibody (1:1000 dilution, mouse monoclonal; Thermo Fisher Scientific Cat# 459230, RRID:AB_2532233; Rockford, IL) to recognize and bind to the protein of interest. The membranes were incubated with anti-mouse horseradish peroxidase (HRP) conjugated

TABLE 2 DsiRNA sequence.

DsiRNA	Duplex sequence
SDHB.R1	5′-GAUUGACACCAACCUCAAUAAGGTC-3′
	3′-UCCUAACUGUGGUUGGAGUUAUUCCAG-5′
SDHB.R2	5′-AUGAAGUUGACUCUACUUUGACCTT-3′
	3′-CUUACUUCAACUGAGAUGAAACUGGAA-5′
SDHB.R3	5′-UUUCCAUGAAUACAGCAUGUAUAAT-3′
	3′-CAAAAGGUACUUAUGUCGUACAUAUUA-5′

TABLE 3 List of primers used for qPCR.

Gene name	Primer name	Primer sequence
SDHB	SDHB-F	5′-GCAGTCCATAGAAGAGCGTGAG-3′
	SDHB-R	5′-TGTCTCCGTTCCACCAGTAGCT-3′
RPS16	RPS16-F	5′-GTCTGTGCAGGTCTTCGGACGC-3′
	RPS16-R	5′-GACCATTGCCGCGTTTGCAGTG-3′

secondary antibody (1:7500; Jackson ImmunoResearch Labs Cat# 115-035-003, RRID:AB_10015289), for 1 h at room temperature, to detect the primary antibody and amplify the signal for detection. Bands were developed by incubating the membranes in chemiluminescent SuperSignal West Dura Extended Duration Substrate (Thermo Fisher Scientific, Rockford, IL) for 3 min and visualized using the ChemiDoc MP imaging system. The intensities of all the separated protein bands in the stain-free gels and the band intensity of the protein of interest in the membranes, within each lane, were then analyzed using the Image Lab software (version 6.0.1; RRID:SCR_014210; Bio-Rad, Hercules, CA). The band intensity of the protein of interest was normalized to the total protein loaded in their respective lanes. The amount of total protein loaded in each lane was measured from the stain-free gel by quantifying the cumulative intensities of all individual protein bands in the lane. The relative band intensity of the protein of interest from each patient was further normalized to their respective controls. In a previous study, quantification of total protein per band was verified by systematic dilution of the lysate thereby changing the amount of protein loaded, then probing the blot with RPS16.[45] We confirmed that levels of RPS16 corresponded to the total protein loaded in the lane. Importantly, normalization to total protein per lane makes no assumptions regarding the lack of an effect on housekeeping proteins. All gel and full blot images are provided in the Figures S2–S4.

2.9 | Measurement of oxygen consumption rate (OCR) by respirometry

hASM cells were plated into the Seahorse XFe24 cell culture microplates (Agilent Technologies, Santa Clara, CA, USA) as recommended by the manufacturer for optimal adherence and growth of mammalian cells. hASM cells were then incubated to allow for cell adherence and formation of a confluent monolayer. Following exposure to malonate or SDHB knockdown, the cells were serum-deprived. Oxygen consumption rate (OCR) was measured by the mitochondrial stress test assay performed using the Agilent Seahorse XFe24 Cell Analyzer (RRID:SCR_019539; Agilent Technologies, Santa Clara, CA, USA) as per the manufacturer's instructions and as described previously.[12,16] On the day of the assay, the serum-free media was replaced with the recommended seahorse assay medium, Seahorse XF DMEM base medium (Agilent, Santa Clara, CA, USA), supplemented with 10 mM glucose, 1 mM sodium pyruvate, and 2 mM glutamine at pH 7.4 and maintained in a 37°C CO_2-free incubator for 1 h. Prior to the assay, the Seahorse Xfe24 FluxPak sensor cartridge was hydrated using Seahorse XF calibrant solution for 12–24 h. The ETC complex inhibitors and FCCP were loaded into the injection ports on the sensor cartridge at optimal concentrations determined for hASM cells, which are as follows: 1 μM oligomycin (ATP uncoupler), 1.25 μM FCCP (accelerates electron transport chain), and 1 μM antimycin A (Complex III inhibitor) with 1 μM rotenone (Complex I inhibitor).[46-51] This allowed for the determination of basal respiration, ATP production, maximum respiration, and spare respiratory capacity. All OCR measurements were normalized to total adherent cell count, obtained before assaying.[18,52] The total number of cells within each well was obtained by *in situ* cell counting prior to every mitochondrial stress test using 1 μg/mL Hoechst 33342 Solution (Invitrogen, Carlsbad, CA, USA; excitation/emission wavelength: 361/486 nm) and Cytation 5 Cell Imaging Multi-Mode Reader (RRID:SCR_019732; BioTek, Winooski, VT, USA). All data were analyzed using Seahorse Wave software (version 2.6.3; RRID:SCR_014526; Agilent Technologies, Santa Clara, CA, USA). hASM cells from the same six patients were used for OCR measurement (4 wells/patient).

2.10 | Transduction-mediated labeling of mitochondria in hASM cells

hASM cells were plated at a density of ~15,000 cells/well into 8-well Ibidi μ-slide plates (Ibidi GmbH, Gewerbehof Gräfelfing, Germany) and incubated to allow for cell adherence. Adhered hASM cells were transduced with CellLight™ Mitochondria-GFP, Bac-Mam 2.0 (Invitrogen, Carlsbad, CA, USA) to label the mitochondria, as per the manufacturer's instructions. This is a baculovirus system with a fusion construct of the leader sequence of E1 alpha pyruvate dehydrogenase and emGFP, providing accurate and specific targeting to cellular mitochondria.[53] hASM cells were incubated in growth media containing CellLight for 24 h at 37°C. Subsequently, the hASM cells were washed with 1X PBS and serum-deprived for 48 h. Although the efficiency of transduction was relatively low (~60%), GFP protein could be observed in the mitochondria.

2.11 | Confocal imaging of mitochondria in hASM cells

Mitochondria in hASM cells were imaged using the same confocal microscope system used for SDH measurements as described above.[16-18,54,55] The dynamic range for imaging was set by first scanning a region containing no fluorescence signal and then a second region containing maximum fluorescence signal. A series of 0.5 μm optical

slices were acquired for each hASM cell to obtain a Z-stack, using the NIS-Elements software. Multiple hASM cells (identified by size and elongated shape) were visualized within a single microscopic field. Due to the large size of hASM cells, the borders of some cells overlapped, and only those hASM cells whose borders were not overlapping were included. Typically, this selection process resulted in the analysis of 2–3 hASM cells per field.

2.12 | Mitochondrial volume density

The 3D images obtained were deconvolved using the automatic deconvolution algorithm on NIS-Elements software (Modified Richardson Lucy method; Point Scan Confocal modality; Nikon Instruments Inc.; version 5.20.02; RR ID:SCR_014329).[16,18,55,56] Deconvolution enhances the signal-to-noise ratio in the images, thereby improving contrast and edge detection. The voxel dimensions of each deconvolved optical slice were $0.207 \times 0.207 \times 0.5\,\mu m$. After deconvolution, the boundaries of each hASM cell were delineated and ROI was defined in ImageJ-Fiji software (https://imagej.nih.gov/ij/; version 1.53t, RRID:SCR_002285; NIH, Public Domain). Using the mitochondrial analyzer plugin (https://github.com/AhsenChaudhry/Mitochondria-Analyzer) available on ImageJ, the Z-stacks were then processed for background correction and ridge filter detection.[16,54,57-59] The mitochondria within hASM cells were identified by thresholding to create a binary image and then skeletonized for morphometric analysis. Using the thresholded binary image, total mitochondrial volume was measured by the mitochondrial analyzer plugin where the number of voxels containing fluorescently labeled mitochondria within an ROI was determined.[54,60] Mitochondrial volume density was calculated as the ratio of mitochondrial volume within an ROI to the total volume of the defined ROI (mean cross-sectional area of the ROI from all optical slices × total number of slices × 0.5 µm) and represented as a percentage of the volume of the ROI.[9-11,16,55,56] Based on an *a priori* power analysis of variance in mitochondrial volume density measurements in untreated hASM cells, $n = 5$ individual hASM cells per bronchiolar sample (from six patients) were included in the analysis.

2.13 | Mitochondrial complexity index (MCI)

Mitochondrial morphological parameters, including mitochondrial volume and mitochondrial surface area, were measured in hASM cells as described above. The extent of mitochondrial fragmentation was assessed by calculating the mitochondrial complexity index (MCI) using the following equation[9,11,61]:

$$\mathrm{MCI} = \frac{\mathrm{SA}^3}{16\pi^2 V^2}$$

where SA is the total mitochondrial surface area measured within the ROI and V is the total volume occupied by the mitochondria within the ROI. More fragmented mitochondria exhibit lower surface area, higher volume and thus, lower MCI.

2.14 | Mitochondrial distribution within hASM cells

To simultaneously measure SDH_{max} relative to mitochondrial volume within different compartments of hASM cells, mitochondria were labeled using CellLight™ Mitochondria-GFP (Figure 5A–C). During 3D imaging of labeled mitochondria, sampling depth was restricted to 5 µm in the Z-axis (2.5 µm above and below the nuclear centroid) with a fixed optical slice thickness of 0.5 µm (Figure 5D). During SDH_{max} measurements, Z-stacks were obtained at 15 s intervals over an 8-min period. Mitochondrial volume density was analyzed with respect to distance from the nuclear membrane using a concentric shell method of analysis, similar in principle to a Sholl Analysis. After deconvolution of each optical slice, thresholding was applied to the space corresponding to the nucleus and the nuclear membrane was delineated using an edge detection-based threshold algorithm on ImageJ-Fiji (version 1.53t, RRID:SCR_002285). The SNT Sholl Analysis plugin (https://github.com/morphonets/SNT) available on ImageJ was used to perform semiautomated processing of the Z-stacks to create concentric shells radiating at 10 µm intervals from the outer edge of the nuclear membrane and radiating outwards in 3D at 10 µm intervals to a maximum distance of 120 µm from the nuclear membrane (Figure 5E). Mitochondria within each shell were identified by thresholding to create a binary image and then skeletonized for morphometric analysis. Within each shell, voxels containing fluorescently labeled mitochondria were distinguished from those displaying no fluorescence and mitochondrial volume density and MCI were determined using the mitochondrial analyzer plugin as described above. Within the corresponding 3D shells, SDH_{max} within the volume of each shell was determined as described above. All images were obtained with cells equilibrated at room temperature (25°C). This temperature was chosen as it dramatically slows the movement of mitochondria.[18] This is important when acquiring image stacks, to avoid the same mitochondria from appearing in different focal planes, which can lead to a false impression of the size and connectivity of the organelles. Additionally, as the measurement of mitochondrial

volume density in the more distal shells (80–120 μm) posed considerable variability, only the shells with low variance in mitochondrial volume density (≤60 μm) were considered for analysis.

2.15 | Validation of antibodies

Validation of the antibodies used in the present study was based on previous work from our laboratory as well as other laboratories, and datasheets provided by vendors.[12,21,23,24,45,52,62] The α-SMA antibody was validated using lysates from hASM cells and NSC-34 cell line (non-smooth muscle cell; RRID:CVCL_D356). As expected, a band was observed in hASM cell lysate between the 37 and 50 kDa bands of the protein ladder, which is consistent with the molecular weight of α-SMA (42 kDa). However, this was absent in the NSC-34 cell lysate (Figure S2). As part of the study, by using siRNA-mediated knockdown of SDHB subunit the antibody for SDHB was validated. The expression of SDHB was measured in lysates of hASM cells transfected with three SDHB targeting DsiRNA sequences (R1, R2, and R3) and scrambled DsiRNA as a negative control (NC). Consistent with the molecular weight of SDHB (32 kDa), in the lysates from negative control, a band was observed between the 25 and 37 kDa bands of the protein ladder, whereas in lysates with SDHB-knockdown, a significant decrease in the expression of SDHB was observed for all three sequences (Figures S1 and S3). The antibody for SDHB was further validated by assessing the presence of SDHB immunoreactive bands between mitochondrial and cytosolic fractions of untreated hASM cells. As expected, while there was an immunoreactive band for SDHB present between the 25 and 37 kDa bands of the protein ladder in the mitochondrial fraction, no bands were observed in the cytosolic fraction (Figure S4).

2.16 | Statistical analysis

Sex is an important biological variable; therefore, hASM cells for all experiments were dissociated from bronchial tissue samples obtained from both female and male patients. However, this study was not powered to detect sex differences or past smoking history as major outcome variables, and sex was considered as a random variable in the statistical analysis. Experimenters were not blinded, and hASM cells were not randomized into groups because this was deemed irrelevant for this study. Importantly, hASM cells from the same passage (1–3 passages) and cells from the same patient were distributed into the treatment groups listed in the study and all groups were processed in the same experimental conditions to exclude any batch effects. Therefore, hASM cells from each patient served as their own control. Sample size (n) represents the number of hASM cells analyzed per bronchial sample (patient), and the n used for each experiment is provided in the figure legends. The minimum number of patients and cells per patient used was determined by a power analysis of primary outcome measures. The expected effect size was calculated with an *a priori* biologically relevant difference of 20% and equal variance, with sample size estimated using $d=1.4$, $\alpha=0.05$, and $\beta=0.8$ (5 cells/patient; 6 patients—3 females and 3 males). The experiments were designed such that the comparisons were made within a patient. Statistical analysis was performed using GraphPad Prism 9 (version: 9.5.0, RRID:SCR_002798; San Diego, CA). Normal distribution of data was confirmed using the Shapiro–Wilk test. The linearity of the SDH assay was assessed from a single patient using the simple linear regression model. The mitochondrial volume density, MCI, and corresponding SDH_{max} were assessed from a single patient using a non-linear regression model (curve fit analysis). For all SDH_{max} and OCR measurements, each color represents a single patient. For all experiments, two-way ANOVA for repeated measurements was used to compare treatment groups. The basal outcome measures varied across patient samples; however, patient-to-patient comparison was beyond the scope of the present study. Statistical significance was concluded if $p<0.05$ and was indicated by * in the figures and figure legends.

3 | RESULTS

3.1 | Phenotype of dissociated hASM cells

The cells dissociated from the dissected smooth muscle layer of third to sixth-generation bronchi were immunoreactive to α-SMA (Figure 2A). Consistent with our previous studies,[12,16,24,45,63] a majority of the dissociated cells (90%–95%) displayed immunoreactivity to α-SMA, indicating that they were hASM cells (Figure 2B). These hASM cells were also larger and displayed a characteristic elongated shape that distinguished them from other cells. In all experiments involving quantitative histochemical analysis, the distinct morphological features of the cells were used to identify hASM cells.

3.2 | SDH reaction is linear across time in hASM cells

The linearity of the SDH reaction in hASM cells was confirmed by measuring the change in OD within

delineated hASM cells every 15 s across an 8-min period (Figure 3A). Within the hASM cells, the reaction progressed in a linear fashion from 0 to 8 min with the progressive accumulation of NBT_{dfz} (change in OD; $R^2 = 0.99$; Figure 3B). The change in OD was measured in the absence of any succinate (without substrate), where the reaction was linear with respect to the time of incubation ($R^2 = 0.95$). The change in OD without succinate was significantly lower compared to the change in OD in the presence of succinate ($p < 0.0001$; Figure 3B). The change in OD in the absence of cells (buffer blanks) was also measured and found to be unchanged throughout the time of incubation.

3.3 | SDH inhibition decreases SDH_{max} in hASM cells

The specificity of the SDH reaction was validated by inhibiting the catalytic core of SDH, SDHA, and SDHB. SDH_{max} was measured in hASM cells treated with malonate (1 mM for 24 h), a competitive inhibitor of SDH that can inhibit succinate uptake by binding to the carboxylate site of SDHA subunit (Figure 4A).[39-42] SDH_{max} was significantly decreased in malonate-treated hASM cells when compared to untreated (control) hASM cells (*$p < 0.0001$; Figure 4B). For comparison, the maximal respiration rates were obtained from the OCR measurements for malonate-treated and control hASM cells (Figure 4C). The maximal respiration rate was significantly decreased in malonate-treated hASM cells when compared to control hASM cells (*$p < 0.001$; Figure 4D).

SDHB knockdown was generated by transfecting hASM cells with DsiRNA targeted to SDHB (Figure 4E). Effective transfection was first confirmed by using TYE563, with which fluorescence was observed within the hASM cells up to 72 h post-transfection (Figure S1A). After establishing an optimal transfection protocol, hASM cells were transfected with three SDHB targeting DsiRNA sequences, siRNA.R1, siRNA.R2, and siRNA.R3, and scrambled siRNA as negative control (NC). Following transfection, the knockdown was confirmed by qPCR (Figure S1B,C) and western blot (Figure S1D–F) in all the patients. Quantified data showed a significant decrease in both mRNA and protein expression of SDHB for all three sequences compared to NC (*$p < 0.05$). The sequence (siRNA.R3) that produced the highest percentage of knockdown (~90%) out of the three DsiRNA sequences was used for further experiments. SDH_{max} measured in SDHB-knockdown (SDHB-KD) hASM cells was significantly decreased compared to NC (*$p < 0.0001$; Figure 4F). For comparison, the maximal respiration rate was obtained from the OCR measurements for SDHB-KD and NC hASM cells (Figure 4G). The maximal respiration rate was significantly decreased in SDHB-KD hASM cells when compared to NC (*$p < 0.0001$; Figure 4H).

3.4 | NBT_{dfz} distribution corresponds to mitochondrial localization within hASM cells

The pattern of distribution of mitochondria and NBT_{dfz} accumulation within perinuclear and distal compartments of hASM cells was determined (Figure 5A–D). To analyze the mitochondrial distribution within hASM cells, CellLight-labeled mitochondria within hASM cells were imaged in 3D and mitochondrial volume density was measured within concentric shells (Figure 5A,E). Consistent with our previous findings,[16] a predominance of mitochondria volume within the perinuclear region of hASM cells was observed as evidenced by the higher percentage of mitochondria at distances closer to the nuclear membrane. Approximately 60% of all mitochondria were located within 20 μm of the nuclear membrane of the hASM cell (Figure 5F). SDH_{max} was measured within the same cells, and the distribution of NBT_{dfz} was assessed (Figure 5B,E). Similar to the distribution of mitochondria, accumulation of NBT_{dfz} was higher in the perinuclear compartment, where ~2-fold higher SDH_{max} was observed within 20 μm of the perinuclear area when compared to the distal regions of the hASM cell (≥40 μm; Figure 5F). When compared, the curves obtained for mitochondrial volume density and SDH_{max} correspond but do not completely overlap. When SDH_{max} from each shell were normalized to their respective mitochondrial volumes, the SDH_{max} per mitochondrion in the perinuclear region (≤20 μm) was decreased ~2-fold when compared to the distal compartments (≥40 μm; Figure 5G). To assess changes in mitochondrial morphology within hASM cells relative to the distance from the nuclear membrane, we employed the MCI as a three-dimensional metric of complexity of mitochondrial morphology.[61] The MCI was decreased by ~6-fold at 60 μm from the nuclear membrane when compared to the MCI within 10 μm of the nuclear membrane (Figure 5H). Overall, the data indicated a significant reduction in the MCI in the distal parts of the cell indicating that mitochondria are more filamentous around the perinuclear area and more fragmented in the distal parts of the cell.

4 | DISCUSSION

In the present study, we investigated the extent of morphological and functional heterogeneity of mitochondria in hASM cells by simultaneous confocal imaging

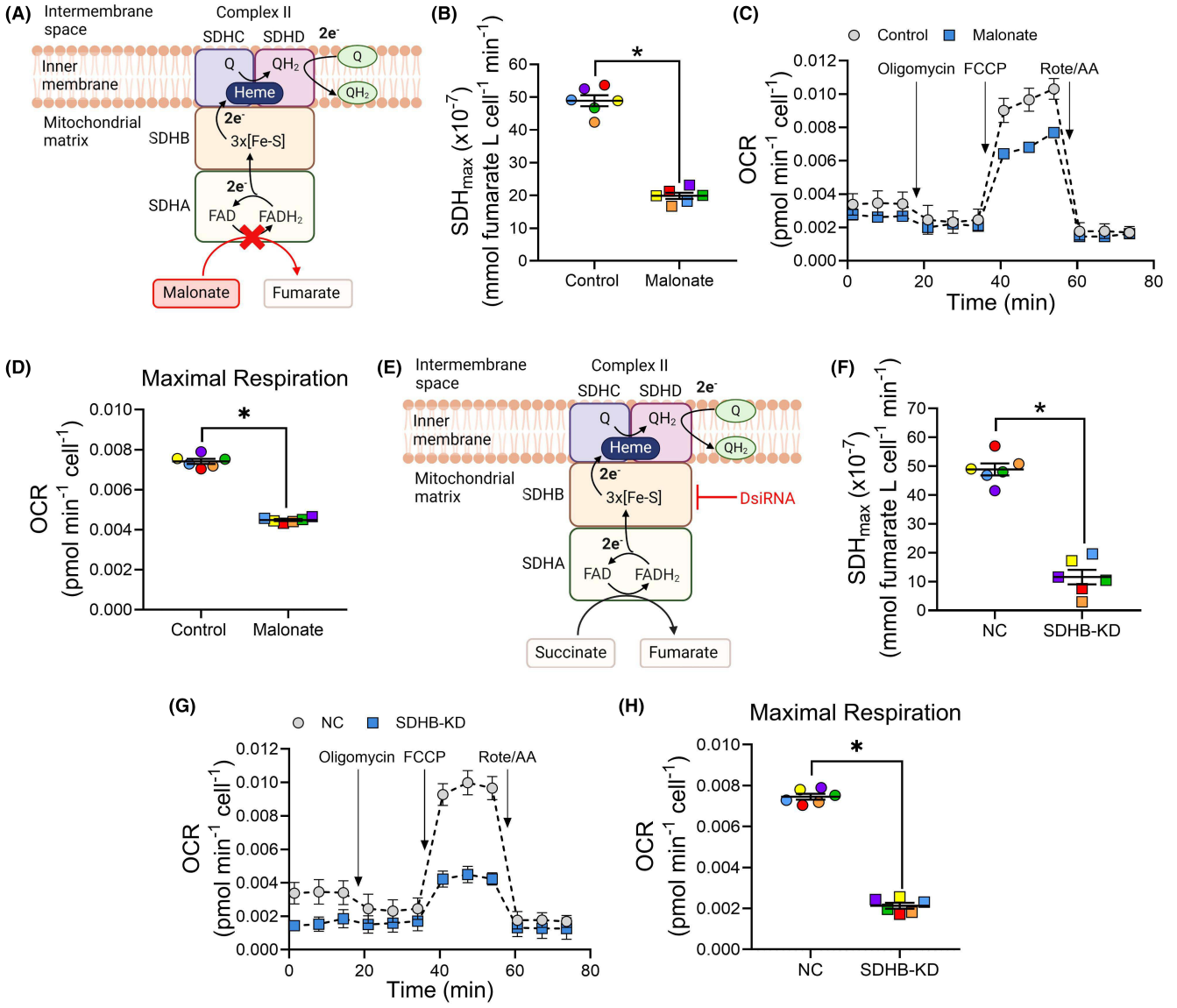

FIGURE 4 Inhibition of SDH catalytic core decreases SDH_{max}. (A) The diagram shows malonate competitively inhibiting SDH by blocking succinate uptake (Created with BioRender.com). (B) SDH_{max} measured in hASM cells after malonate treatment (1 mM for 24 h) was significantly decreased when compared to untreated (control) hASM cells (*$p < 0.0001$). (C) OCR measurements obtained from malonate-treated and control hASM cells were normalized to the total cell count. (D) The maximal respiration was significantly decreased in malonate-treated cells when compared to control hASM cells (*$p < 0.0001$). Each color represents results from one bronchial sample (patient). Circles represent SDH_{max} from untreated (control) hASM cells, and squares represent SDH_{max} from malonate-treated cells. (E) The diagram shows the inhibition of the B subunit of SDH by targeted DsiRNA-mediated knockdown (Created with BioRender.com). hASM cells were transfected with DsiRNA targeting SDHB (SDHB-KD), with scrambled DsiRNA as negative control (NC). (F) SDH_{max} measured was significantly decreased in SDHB-KD hASM cells when compared to NC (*$p < 0.0001$). (G) OCR measurements obtained from SDHB-KD cells and NC cells were normalized to total cell count. (H) The maximal respiration was significantly decreased in SDHB-KD hASM cells when compared to NC (*$p < 0.0001$). Each color represents results from one bronchial sample (patient). Circles represent SDH_{max} from NC hASM cells, and squares represent SDH_{max} from SDHB-KD cells. Data are presented as mean ± SEM in scatter plot. Statistical analyses were based on measurements from $n = 5$ hASM cells per group from six bronchial samples (patients) using two-way ANOVA for repeated measures. hASM, human airway smooth muscle; OCR, oxygen consumption rate; SDH, succinate dehydrogenase.

of fluorescently labeled mitochondria and assessment of SDH activity. The key findings of the present study were as follows: (1) Mitochondrial volume density varied within different compartments of hASM cells, where mitochondrial volume density was higher in the perinuclear region of the cell when compared to the more distal compartments. (2) The morphometry of mitochondria within hASM cells varied significantly, being more filamentous in the perinuclear region of the cell when compared to the distal regions. (3) SDH_{max}

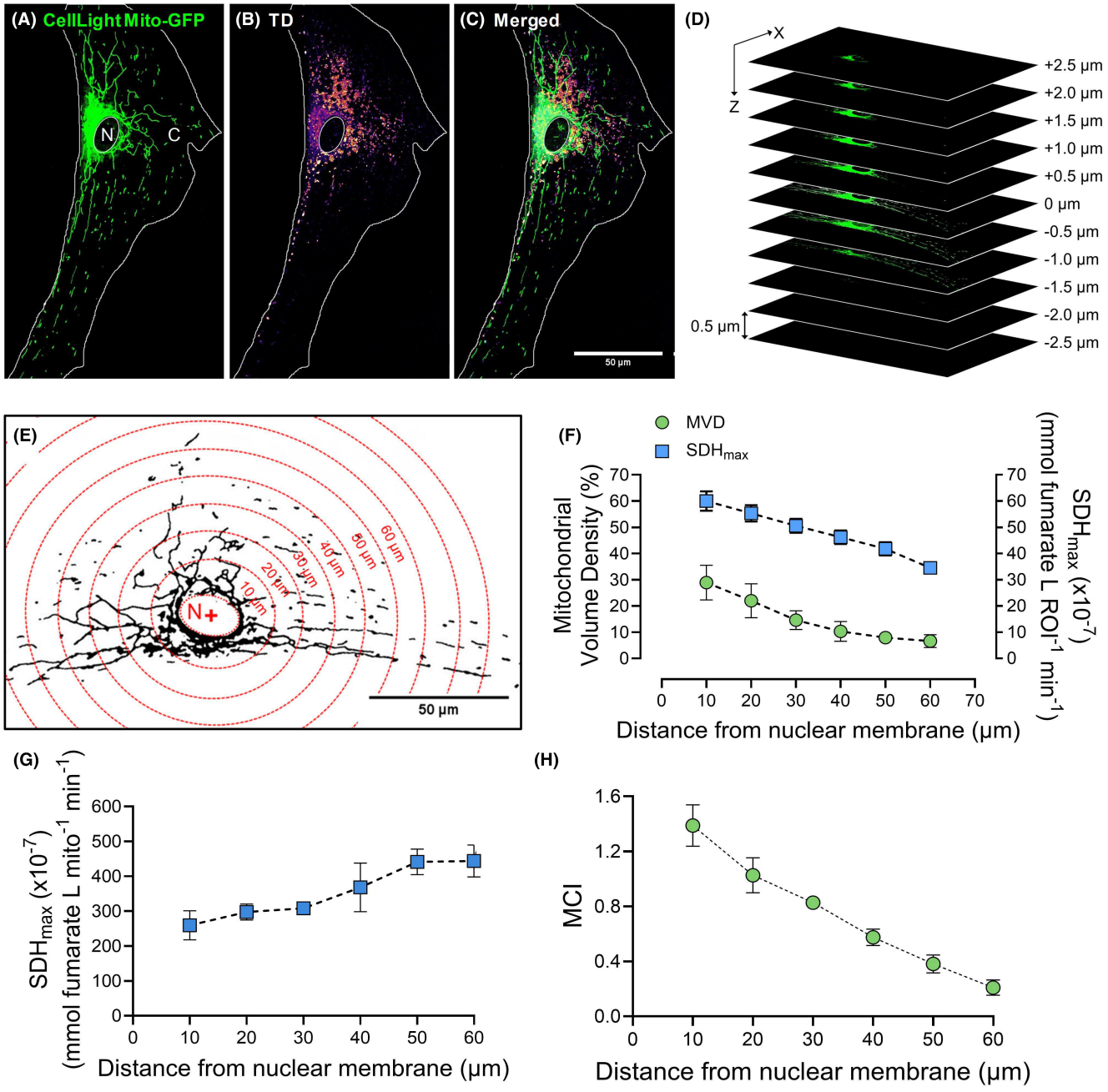

FIGURE 5 NBT_{dfz} accumulation corresponds to mitochondrial volume within hASM cells. (A) Representative maximum intensity Z-projection image of hASM cell loaded with CellLight™ Mitochondria-GFP to visualize mitochondria (scale bar = 50 µm). (B) Representative image (TD) shows NBT_{dfz} accumulation at 8 min. To aid in visualizing the NBT_{dfz} accumulation within hASM cells, the original gray-scale images were manually thresholded and the LUTs were inverted to be represented as a heat map using NIS-Elements software. (C) Overlay of the CellLight-labeled mitochondria and NBT_{dfz} accumulation shows their respective pattern of distribution within the cell. (D) Z-stacks were obtained with a controlled step size of 0.5 µm between optical slices across a 5 µm sampling depth (10 optical slices). (E) Representative image shows the binarized mitochondria within hASM cell with digitally computed and superimposed 3D concentric shells spaced in increments of 10 µm from the nuclear membrane (scale bar = 50 µm; N: Nucleus; +: Nuclear Centroid). Using this, the MCI, mitochondrial volume density and SDH_{max} within each shell were quantified. (F) The distribution of mitochondria as mitochondrial volume density (%) and SDH_{max} within the volume of each shell decreased relative to the distance (in µm) from the nuclear membrane. The SDH_{max} measurements mirrored the mitochondrial volume within the corresponding shells. (G) SDH_{max} normalized to mitochondrial volume decreased ~2-fold in the perinuclear region when compared to those in the distal region. (H) MCI within the volume of each shell increased ~6-fold in the perinuclear region when compared to the distal compartments. Circles represent mitochondrial volume density and MCI, and squares represent SDH_{max}. Statistical analyses in hASM cells were based on measurements from $n = 10$ hASM cells per group from one bronchial sample (patients). hASM, human airway smooth muscle; TD, transmitted light differential interference; MCI, mitochondrial complexity index; NBT, nitroblue tetrazolium diformazan; SDH, succinate dehydrogenase.

also varied within different compartments of hASM cells, where SDH_{max} was greater in the perinuclear region of the cell versus the distal compartments and corresponded to the distribution of mitochondrial volume. (4) When normalized to mitochondrial volume, SDH_{max} was lower in the perinuclear region when compared to the distal regions. This is a surprising observation and would suggest distinct metabolic differences depending on mitochondrial localization within a cell.

4.1 | Quantitative histochemical technique to measure SDH_{max}

The technique for measuring SDH_{max} was initially developed and first reported in 1986 by Sieck et al.,[5] followed by a subsequent publication that provided greater detail.[6] The quantitative histochemical technique measures the progressive reduction of NBT (reaction indicator) to its diformazan state (NBT_{dfz}). The reaction is performed using mPMS as an exogenous electron carrier and azide to inhibit cytochrome oxidase (Complex IV). mPMS is reduced within complex II and azide inhibits complex IV preventing the subsequent re-oxidation of mPMS. This allows mPMS to preferentially deliver electrons to NBT and minimize any non-specific reduction of NBT.[64] The optimal concentrations of the various compounds used in the assay were rigorously determined in previous studies.[5-11,13,25-35,65,66] In the quantitative histochemical method for measuring SDH_{max}, the Beer–Lambert equation is used which requires the control of path length for light absorbance to determine the accumulation of the reaction product (i.e., NBT_{dfz}). In measuring SDH_{max} in skeletal muscle fibers, the path length for light absorbance is controlled by cryo-sectioning the fibers at a defined thickness.[9-11,13] As cryo-sectioning is difficult in single cells such as hASM cells, we validated the use of confocal microscopy to acquire optical slices, thereby controlling path length for light absorbance.[12] In the quantitative histochemical technique, it is essential to use an optimal concentration of succinate (substrate) to avoid substrate limiting the reaction. Consistent with our previous study, we found that SDH_{max} in hASM cells was achieved at a succinate concentration of 80 mM in the reaction media.[12] Furthermore, we confirmed that the SDH reaction is linear over an 8-min period in hASM cells, which is similar to that observed in skeletal muscle fibers.[5,6,9,11,13] Therefore, at maximum substrate concentration, the reaction proceeds in a linear fashion from which the maximum velocity can be determined.

In the present study, the specificity of the SDH assay was further validated by inhibiting the catalytic core of the SDH complex, namely SDHA and SDHB subunits. SDH is a holoenzyme consisting of four nuclear-encoded protein subunits. The catalytic core, SDHA and SDHB subunits, contain the binding/catalytic site that binds to organic substrates, succinate or fumarate, and the redox cofactors that participate in electron transfer to ubiquinone.[1-4,37,38] The membrane domain, SDHC and SDHD subunits, anchors the complex to the IMM.[1-4,37,38] Malonate-mediated competitive inhibition of SDHA in hASM cells as well as siRNA-mediated SDHB knockdown decreased SDH_{max} which was consistent with the reduction of maximum OCR. These results are also consistent with other reports where SDH metabolism was studied using biochemical methods.[2,67-71]

4.2 | Distribution of mitochondrial volume varies within hASM cells

In the present study, using 3D confocal imaging, fluorescently labeled mitochondria were identified and mitochondrial volume density was measured within hASM cells. Previously, we compared the use of 3D confocal imaging to determine mitochondrial volume to that obtained by electron microscopy (EM) and found them to be comparable.[55] Mitochondrial labeling with MitoTracker Green and 3D imaging have a major advantage over EM in that many cells can be analyzed per sample, and MitoTracker allows measurements from living cells and metabolically active mitochondria. Importantly, as SDH_{max} can vary with changes in mitochondrial volume density, normalizing SDH_{max} to mitochondrial volume provides valuable information on the relationship between mitochondrial structure and function.[11-13] Unfortunately, simultaneous measurements of SDH_{max} and mitochondrial imaging by MitoTracker labeling are not possible in hASM cells since MitoTracker interferes with SDH_{max} measurements.[12] Therefore, CellLight was used as an alternative to label mitochondria and we confirmed that, unlike MitoTracker Green, CellLight labeling does not affect SDH_{max} measurements.[12] CellLight is a BacMam expression vector encoding GFP fused to the leader sequence of E1α pyruvate dehydrogenase and labels independently of the mitochondrial membrane potential.[53,72,73]

Using a concentric shell analysis, we determined differences in mitochondrial volume density within perinuclear to distal compartments of an hASM cell. Consistent with previous findings, we observed that mitochondrial volume density was highest within ~20 μm of the nuclear membrane and then decreased toward the more distal compartments of the hASM cell.[16] Similar observations were made in other transformed cell lines and primary cell types, where mitochondria were distributed throughout the cytosol but had a higher density in the perinuclear region.[74-77]

4.3 | Mitochondrial morphometry is heterogeneous within hASM cells

Using the same concentric shell analysis, mitochondrial morphology was quantified by MCI and varied significantly within hASM cells. The mitochondrial network within hASM cells comprised both elongated mitochondrial networks as well as fragmented/globular mitochondria, thereby contributing to considerable variance in the metrics of mitochondrial morphology (MCI). Within hASM cells, more elongated/filamentous mitochondrial networks were present in the perinuclear compartments and transitioned toward more fragmented mitochondria in the distal regions of the cell. The presence of such distinct differences in mitochondrial morphology within different cells have been presented in various cell types.[75] Mitochondrial morphology is highly dynamic and is closely coordinated with its function. Mitochondria undergo membrane remodeling through cycles of fragmentation and fusion; the balance of these processes controls mitochondrial metabolism during normal mitochondrial turnover in homeostasis and in response to mitochondrial or cellular stress.[78,79] Numerous studies have explored the relationship between mitochondrial morphology and function, and its correlation with the cellular energy demand.[80] It is observed that fused mitochondria promote the formation of elongated mitochondrial networks which contain intricate cristae organization, therefore enhancing the ATP output and oxidative phosphorylation.[81] On the other hand, small or fragmented mitochondria are relatively poor ATP producers and less reliant on oxidative phosphorylation.[82] The asymmetric distribution of mitochondrial volume and morphology within hASM cells suggests a possible difference in metabolic demand within different compartments of the cell.

4.4 | SDH_{max} corresponds with mitochondrial volume within hASM cells

In the present study, SDH_{max} was simultaneously measured within hASM cells with CellLight-labeled mitochondria. In previous findings, we reported a strong relationship between SDH_{max} and CellLight-labeled mitochondrial volume density in hASM cells.[12] During the course of the SDH reaction, a more rapid accumulation of NBT_{dfz} is observed in regions corresponding to higher mitochondrial volume density within hASM cells. Using the concentric shell analysis, we determined differences in SDH_{max} relative to the nuclear membrane within various compartments of an hASM cell. Similar to mitochondrial volume density, SDH_{max} was highest within ~20 μm of the nuclear membrane and then decreased toward the more distal compartments of the hASM cell, with significant correspondence in distribution pattern between NBT_{dfz} accumulation and mitochondrial volume. Consistent with the changes in mitochondrial morphometry within the cells, the higher SDH_{max} measured in the perinuclear compartment reflects the more filamentous morphometry of mitochondria in the perinuclear compartment, whereas the lower SDH_{max} reflects the fragmented morphometry of mitochondria in the distal compartments. In previous studies, we reported that mitochondrial motility is more pronounced in the perinuclear region within hASM cells, with increased mitochondrial Ca^{2+} influx in the perinuclear region when compared to the more distal compartments of the cell.[17,18]

Interestingly, SDH_{max} normalized to mitochondrial volume was lower in the perinuclear region (within ~20 μm of the nuclear membrane) and increased toward the more distal parts of the cell. Provided SDH complex, along with other ETC complexes, is embedded within the IMM, the surface area of the IMM can influence the functional capacity of mitochondria to consume oxygen, pump protons, and produce ATP.[15] Studies have shown that as the IMM expands, cristae formation is promoted, therefore expanding the space needed for the cell to increase the number of ETC complexes present in the organelle and increasing the capacity of the mitochondria to produce ATP.[83,84] However, this is in contrast to our observations, as lower SDH_{max} per mitochondrion is observed in the perinuclear area which consists of filamentous mitochondria. This can be attributed to the fact that in the perinuclear region of many cells, the filamentous mitochondria present are not luminally interconnected, therefore consisting of different matrix densities within individual mitochondria, reflecting differences in metabolic states.[75] Additionally, similar findings regarding intracellular functional heterogeneity of mitochondria have been made in other cell types. Observation from JC-1 emissions suggests that the distal mitochondria have higher mitochondrial membrane potential ($\Delta\Psi_m$) than their perinuclear counterparts and was further substantiated by the increased Ca^{2+} influx in the distal mitochondria than those in the perinuclear region.[75] These observations indicate that there are proportionally more metabolically active mitochondria in the distal compartments of cells when compared to those in the perinuclear region. In contrast to these observations, the proximity between mitochondria and the nuclear envelope is maintained by the high-energy demands of the nucleus which is met by the mitochondria.[85,86] However, evidence suggests that the high-energy demand at nuclear-mitochondrial contact sites increases ROS production

and accumulation in the perinuclear region thereby disrupting the $\Delta\Psi_m$ and resulting in responses that stimulate mitochondrial turnover, that is, mitophagy and mitochondrial biogenesis.[77,87] While SDH_{max} could be affected by the ROS-mediated mitophagy in the perinuclear region or a decrease in IMM area, understanding the mechanisms underlying the differences in SDH activity and mitochondrial morphology between perinuclear and distal regions is outside the scope of this study and will be explored in future studies.

5 | SUMMARY AND CONCLUSION

In the present study, we demonstrate that mitochondria display a wide range of morphologies that are functionally heterogeneous. Our results provide evidence of a difference in mitochondrial volume and mitochondrial morphology relative to their localization within a cell. Additionally, we show that the SDH assay can be used to probe differences in SDH activity within multiple cellular compartments and conclude that SDH activity varies with mitochondrial volume within the cell. While our measurements represent the steady-state situation, the plasticity of these organelles can result in discrepant observations of heterogeneity/homogeneity in function under adverse conditions. Using the SDH assay, measurement of differences in SDH activity in multiple cellular compartments within a cell can help underscore the functional status of mitochondria within an individual cell under homeostatic and disease conditions.

AUTHOR CONTRIBUTIONS

S. Mahadev Bhat and **G.C. Sieck** conceived and designed research; **S. Mahadev Bhat** performed experiments; **S. Mahadev Bhat** analyzed data; **S. Mahadev Bhat** and **G.C. Sieck** interpreted results of experiments; **S. Mahadev Bhat** prepared figures; **S. Mahadev Bhat** and **G.C. Sieck** drafted manuscript; **S. Mahadev Bhat** and **G.C. Sieck** approved the final version of the manuscript.

ACKNOWLEDGMENTS

We thank Jeffrey Bailey and Dr. Heather Gransee for their technical assistance in the completion of this project.

FUNDING INFORMATION

This work was supported by National Institutes of Health grants R01-HL157984 (G.C.S.).

DATA AVAILABILITY STATEMENT

The raw data supporting the conclusions of this article will be made available by the authors, without undue reservation.

DISCLOSURES

The authors declare that the research was conducted in the absence of any commercial or financial relationships that could be construed as a potential conflict of interest.

ORCID

Sanjana Mahadev Bhat https://orcid.org/0000-0002-7597-9597
Gary C. Sieck https://orcid.org/0000-0003-3040-9424

REFERENCES

1. Cecchini G. Function and structure of complex II of the respiratory chain. *Annu Rev Biochem*. 2003;72:77-109.
2. Benit P, Goncalves J, El Khoury R, et al. Succinate dehydrogenase, succinate, and Superoxides: a genetic, epigenetic, metabolic, environmental explosive crossroad. *Biomedicines*. 2022;10:1788.
3. Rustin P, Munnich A, Rotig A. Succinate dehydrogenase and human diseases: new insights into a well-known enzyme. *Eur J Hum Genet*. 2002;10:289-291.
4. Rutter J, Winge DR, Schiffman JD. Succinate dehydrogenase—assembly, regulation and role in human disease. *Mitochondrion*. 2010;10:393-401.
5. Sieck GC, Sacks RD, Blanco CE, Edgerton VR. SDH activity and cross-sectional area of muscle fibers in cat diaphragm. *J Appl Physiol (1985)*. 1986;60:1284-1292.
6. Blanco CE, Sieck GC, Edgerton VR. Quantitative histochemical determination of succinic dehydrogenase activity in skeletal muscle fibres. *Histochem J*. 1988;20:230-243.
7. Blanco CE, Micevych PE, Zhan WZ, Sieck GC. Succinate dehydrogenase activity of sexually dimorphic muscles of rats. *J Appl Physiol*. 1995;78:2147-2152.
8. Sieck GC, Fournier M, Prakash YS, Blanco CE. Myosin phenotype and SDH enzyme variability among motor unit fibers. *J Appl Physiol*. 1996;80:2179-2189.
9. Brown AD, Davis LA, Fogarty MJ, Sieck GC. Mitochondrial fragmentation and dysfunction in type IIx/IIb diaphragm muscle fibers in 24-month old fischer 344 rats. *Front Physiol*. 2021;12:727585.
10. Brown AD, Fogarty MJ, Davis LA, Dasgupta D, Mantilla CB, Sieck GC. Mitochondrial adaptations to inactivity in diaphragm muscle fibers. *J Appl Physiol (1985)*. 2022;59:1849-1854.
11. Brown AD, Fogarty MJ, Sieck GC. Mitochondrial morphology and function varies across diaphragm muscle fiber types. *Respir Physiol Neurobiol*. 2022;295:103780.
12. Mahadev Bhat S, Yap JQ, Ramirez-Ramirez OA, Delmotte P, Sieck GC. Cell-based measurement of mitochondrial function in human airway smooth muscle cells. *Int J Mol Sci*. 2023;24:11506.
13. Fogarty MJ, Mathieu NM, Mantilla CB, Sieck GC. Aging reduces succinate dehydrogenase activity in rat type IIx/IIb diaphragm muscle fibers. *J Appl Physiol*. 2020;128:70-77.
14. Heine KB, Parry HA, Hood WR. How does density of the inner mitochondrial membrane influence mitochondrial performance? *Am J Physiol Regul Integr Comp Physiol*. 2023;324:R242-R248.
15. Mannella CA, Lederer WJ, Jafri MS. The connection between inner membrane topology and mitochondrial function. *J Mol Cell Cardiol*. 2013;62:51-57.

16. Delmotte P, Marin Mathieu N, Sieck GC. TNFα induces mitochondrial fragmentation and biogenesis in human airway smooth muscle. *Am J Physiol Lung Cell Mol Physiol*. 2021;320:L137-L151.
17. Delmotte P, Yang B, Thompson MA, Pabelick CM, Prakash YS, Sieck GC. Inflammation alters regional mitochondrial Ca^{2+} in human airway smooth muscle cells. *Am J Physiol Cell Physiol*. 2012;303:C244-C256.
18. Delmotte P, Zavaletta VA, Thompson MA, Prakash YS, Sieck GC. TNFα decreases mitochondrial movement in human airway smooth muscle. *Am J Physiol Lung Cell Mol Physiol*. 2017;313:L166-L176.
19. Prakash YS, Kannan MS, Sieck GC. Regulation of intracellular calcium oscillations in porcine tracheal smooth muscle cells. *Am J Phys*. 1997;272:C966-C975.
20. Prakash YS, Iyanoye A, Ay B, Sieck GC, Pabelick CM. Store-operated Ca^{2+} influx in airway smooth muscle: interactions between volatile anesthetic and cyclic nucleotide effects. *Anesthesiology*. 2006;105:976-983.
21. Aravamudan B, Thompson M, Pabelick C, Prakash YS. Brain-derived neurotrophic factor induces proliferation of human airway smooth muscle cells. *J Cell Mol Med*. 2012;16:812-823.
22. Jia L, Delmotte P, Aravamudan B, Pabelick CM, Prakash YS, Sieck GC. Effects of the inflammatory cytokines TNF-α and IL-13 on stromal interaction molecule–1 aggregation in human airway smooth muscle intracellular Ca^{2+} regulation. *Am J Respir Cell Mol Biol*. 2013;49:601-608.
23. Yap J, Chen X, Delmotte P, Sieck GC. TNFα selectively activates the IRE1α/XBP1 endoplasmic reticulum stress pathway in human airway smooth muscle cells. *Am J Physiol Lung Cell Mol Physiol*. 2020;318:L483-L493.
24. Dasgupta D, Mahadev Bhat S, Price AL, Delmotte P, Sieck GC. Molecular mechanisms underlying TNFα-induced mitochondrial biogenesis in human airway smooth muscle. *Int J Mol Sci*. 2023;24:5788.
25. Sieck GC, Sacks RD, Blanco CE. Absence of regional differences in the size and oxidative capacity of diaphragm muscle fibers. *J Appl Physiol*. 1987;63:1076-1082.
26. Sieck GC, Lewis MI, Blanco CE. Effects of undernutrition on diaphragm fiber size, SDH activity, and fatigue resistance. *J Appl Physiol*. 1989;66:2196-2205.
27. Enad JG, Fournier M, Sieck GC. Oxidative capacity and capillary density of diaphragm motor units. *J Appl Physiol*. 1989;67:620-627.
28. Sieck GC, Blanco CE. Postnatal changes in the distribution of succinate dehydrogenase activities among diaphragm muscle fibers. *Pediatr Res*. 1991;29:586-593.
29. Sieck GC, Cheung TS, Blanco CE. Diaphragm capillarity and oxidative capacity during postnatal development. *J Appl Physiol*. 1991;70:103-111.
30. Lewis MI, Monn SA, Sieck GC. Effect of corticosteroids on diaphragm fatigue, SDH activity, and muscle fiber size. *J Appl Physiol*. 1992;72:293-301.
31. Johnson BD, Sieck GC. Activation-induced reduction of SDH activity in diaphragm muscle fibers. *J Appl Physiol*. 1993;75:2689-2695.
32. Sieck GC, Zhan WZ, Prakash YS, Daood MJ, Watchko JF. SDH and actomyosin ATPase activities of different fiber types in rat diaphragm muscle. *J Appl Physiol*. 1995;79:1629-1639.
33. Proctor DN, Sinning WE, Walro JM, Sieck GC, Lemon PW. Oxidative capacity of human muscle fiber types: effects of age and training status. *J Appl Physiol*. 1995;78:2033-2038.
34. Lattari A, Daood MJ, Sieck GC, Watchko JF. Rat diaphragm oxidative capacity, antioxidant enzymes, and fatigue: newborn versus adult. *Pediatr Res*. 1997;42:60-65.
35. Zhan W-Z, Miyata H, Prakash YS, Sieck GC. Metabolic and phenotypic adaptations of diaphragm muscle fibers with inactivation. *J Appl Physiol*. 1997;82:1145-1153.
36. Zuo Y, Hu J, Xu X, Gao X, Wang Y, Zhu S. Sodium azide induces mitochondria-mediated apoptosis in PC12 cells through Pgc-1α-associated signaling pathway. *Mol Med Rep*. 2019;19:2211-2219.
37. Sun F, Huo X, Zhai Y, et al. Crystal structure of mitochondrial respiratory membrane protein complex II. *Cell*. 2005;121:1043-1057.
38. Yankovskaya V, Horsefield R, Tornroth S, et al. Architecture of succinate dehydrogenase and reactive oxygen species generation. *Science*. 2003;299:700-704.
39. Sipos I, Tretter L, Adam-Vizi V. Quantitative relationship between inhibition of respiratory complexes and formation of reactive oxygen species in isolated nerve terminals. *J Neurochem*. 2003;84:112-118.
40. Tretter L, Patocs A, Chinopoulos C. Succinate, an intermediate in metabolism, signal transduction, ROS, hypoxia, and tumorigenesis. *Biochim Biophys Acta*. 2016;1857:1086-1101.
41. Anastacio MM, Kanter EM, Keith AD, Schuessler RB, Nichols CG, Lawton JS. Inhibition of succinate dehydrogenase by diazoxide is independent of the ATP-sensitive potassium channel subunit sulfonylurea type 1 receptor. *J Am Coll Surg*. 2013;216:1144-1149.
42. Potter VR, Dubois KP. Studies on the mechanism of hydrogen transport in animal tissues: Vi. Inhibitor studies with succinic dehydrogenase. *J Gen Physiol*. 1943;26:391-404.
43. Li C, Zamore PD. RNAi in mammalian cells by siRNA duplex transfection. *Cold Spring Harb Protoc*. 2019;4:286-288.
44. Livak KJ, Schmittgen TD. Analysis of relative gene expression data using real-time quantitative PCR and the $2^{-\Delta\Delta C(T)}$ method. *Methods*. 2001;25:402-408.
45. Dasgupta D, Mahadev Bhat S, Creighton C, Cortes C, Delmotte PF, Sieck GC. Molecular mechanisms underlying TNFα induced mitochondrial fragmentation in human airway smooth muscle cells. *Am J Physiol Lung Cell Mol Physiol*. 2023;24:5788.
46. Perez J, Hill BG, Benavides GA, Dranka BP, Darley-Usmar VM. Role of cellular bioenergetics in smooth muscle cell proliferation induced by platelet-derived growth factor. *Biochem J*. 2010;428:255-267.
47. Dranka BP, Benavides GA, Diers AR, et al. Assessing bioenergetic function in response to oxidative stress by metabolic profiling. *Free Radic Biol Med*. 2011;51:1621-1635.
48. Zhou W, Choi M, Margineantu D, et al. HIF1α induced switch from bivalent to exclusively glycolytic metabolism during ESC-to-EpiSC/hESC transition. *EMBO J*. 2012;31:2103-2116.
49. Mookerjee SA, Gerencser AA, Nicholls DG, Brand MD. Quantifying intracellular rates of glycolytic and oxidative ATP production and consumption using extracellular flux measurements. *J Biol Chem*. 2017;292:7189-7207.
50. Rojas-Morales P, Leon-Contreras JC, Aparicio-Trejo OE, et al. Fasting reduces oxidative stress, mitochondrial dysfunction

and fibrosis induced by renal ischemia-reperfusion injury. *Free Radic Biol Med*. 2019;135:60-67.
51. Lefranc C, Friederich-Persson M, Braud L, et al. MR (mineralocorticoid receptor) induces adipose tissue senescence and mitochondrial dysfunction leading to vascular dysfunction in obesity. *Hypertension*. 2019;73:458-468.
52. Aravamudan B, Kiel A, Freeman M, et al. Cigarette smoke-induced mitochondrial fragmentation and dysfunction in human airway smooth muscle. *Am J Physiol Lung Cell Mol Physiol*. 2014;306:L840-L854.
53. Ames RS, Kost TA, Condreay JP. BacMam technology and its application to drug discovery. *Expert Opin Drug Discov*. 2007;2:1669-1681.
54. Chaudhry A, Shi R, Luciani DS. A pipeline for multidimensional confocal analysis of mitochondrial morphology, function, and dynamics in pancreatic beta-cells. *Am J Physiol Endocrinol Metab*. 2020;318:E87-E101.
55. Fogarty MJ, Rana S, Mantilla CB, Sieck GC. Quantifying mitochondrial volume density in phrenic motor neurons. *J Neurosci Methods*. 2021;353:109093.
56. Rana S, Mantilla CB, Sieck GC. Glutamatergic input varies with phrenic motor neuron size. *J Neurophysiol*. 2019;122:1518-1529.
57. Koopman WJ, Visch HJ, Verkaart S, van den Heuvel LW, Smeitink JA, Willems PH. Mitochondrial network complexity and pathological decrease in complex I activity are tightly correlated in isolated human complex I deficiency. *Am J Physiol Cell Physiol*. 2005;289:C881-C890.
58. Koopman WJ, Visch HJ, Smeitink JA, Willems PH. Simultaneous quantitative measurement and automated analysis of mitochondrial morphology, mass, potential, and motility in living human skin fibroblasts. *Cytometry A*. 2006;69:1-12.
59. Koopman WJ, Distelmaier F, Esseling JJ, Smeitink JA, Willems PH. Computer-assisted live cell analysis of mitochondrial membrane potential, morphology and calcium handling. *Methods*. 2008;46:304-311.
60. Hemel I, Engelen BPH, Luber N, Gerards M. A hitchhiker's guide to mitochondrial quantification. *Mitochondrion*. 2021;59:216-224.
61. Vincent AE, White K, Davey T, et al. Quantitative 3D mapping of the human skeletal muscle mitochondrial network. *Cell Rep*. 2019;26:996-1009.e4.
62. Bancos I, Bida JP, Tian D, et al. High-throughput screening for growth inhibitors using a yeast model of familial paraganglioma. *PLoS One*. 2013;8:e56827.
63. Delmotte P, Yap JQ, Dasgupta D, Sieck GC. Chemical chaperone 4-PBA mitigates tumor necrosis factor alpha-induced endoplasmic reticulum stress in human airway smooth muscle. *Int J Mol Sci*. 2023;24:15816.
64. Simard ML, Mourier A, Greaves LC, Taylor RW, Stewart JB. A novel histochemistry assay to assess and quantify focal cytochrome c oxidase deficiency. *J Pathol*. 2018;245:311-323.
65. Watchko JF, Sieck GC. Respiratory muscle fatigue resistance relates to myosin phenotype and SDH activity during development. *J Appl Physiol*. 1993;75:1341-1347.
66. Boerjan ML, Baarends WM, Ruven HJ. A cytochemical staining procedure for succinate dehydrogenase activity in preovulatory mouse oocytes embedded in low gelling temperature agarose. *J Histochem Cytochem*. 1991;39:135-138.
67. Bouillaud F. Inhibition of succinate dehydrogenase by pesticides (SDHIs) and energy metabolism. *Int J Mol Sci*. 2023;24:4045.
68. Green JD, Narahara HT. Assay of succinate dehydrogenase activity by the tetrazolium method: evaluation of an improved technique in skeletal muscle fractions. *J Histochem Cytochem*. 1980;28:408-412.
69. Kim E, Rath EM, Tsang VH, et al. Structural and functional consequences of succinate dehydrogenase subunit B mutations. *Endocr Relat Cancer*. 2015;22:387-397.
70. Zhang D, Wang W, Xiang B, et al. Reduced succinate dehydrogenase B expression is associated with growth and de-differentiation of colorectal cancer cells. *Tumour Biol*. 2013;34:2337-2347.
71. Aspuria PP, Lunt SY, Varemo L, et al. Succinate dehydrogenase inhibition leads to epithelial-mesenchymal transition and reprogrammed carbon metabolism. *Cancer Metab*. 2014;2:21.
72. Kost TA, Condreay JP, Jarvis DL. Baculovirus as versatile vectors for protein expression in insect and mammalian cells. *Nat Biotechnol*. 2005;23:567-575.
73. Zeng J, Du J, Lin J, Bak XY, Wu C, Wang S. High-efficiency transient transduction of human embryonic stem cell-derived neurons with baculoviral vectors. *Mol Ther*. 2009;17:1585-1593.
74. Chang DT, Honick AS, Reynolds IJ. Mitochondrial trafficking to synapses in cultured primary cortical neurons. *J Neurosci*. 2006;26:7035-7045.
75. Collins TJ, Berridge MJ, Lipp P, Bootman MD. Mitochondria are morphologically and functionally heterogeneous within cells. *EMBO J*. 2002;21:1616-1627.
76. Li A, Gao M, Jiang W, Qin Y, Gong G. Mitochondrial dynamics in adult cardiomyocytes and heart diseases. *Front Cell Dev Biol*. 2020;8:584800.
77. Walker BR, Moraes CT. Nuclear–mitochondrial interactions. *Biomolecules*. 2022;12:427.
78. Cloonan SM, Choi AM. Mitochondria in lung disease. *J Clin Invest*. 2016;126:809-820.
79. Mishra P, Chan DC. Mitochondrial dynamics and inheritance during cell division, development and disease. *Nat Rev Mol Cell Biol*. 2014;15:634-646.
80. Madan S, Uttekar B, Chowdhary S, Rikhy R. Mitochondria lead the way: mitochondrial dynamics and function in cellular movements in development and disease. *Front Cell Dev Biol*. 2021;9:781933.
81. Mishra P, Carelli V, Manfredi G, Chan DC. Proteolytic cleavage of Opa1 stimulates mitochondrial inner membrane fusion and couples fusion to oxidative phosphorylation. *Cell Metab*. 2014;19:630-641.
82. Mizumura K, Cloonan SM, Nakahira K, et al. Mitophagy-dependent necroptosis contributes to the pathogenesis of COPD. *J Clin Invest*. 2014;124:3987-4003.
83. Colina-Tenorio L, Horten P, Pfanner N, Rampelt H. Shaping the mitochondrial inner membrane in health and disease. *J Intern Med*. 2020;287:645-664.
84. Nielsen J, Gejl KD, Hey-Mogensen M, et al. Plasticity in mitochondrial cristae density allows metabolic capacity modulation in human skeletal muscle. *J Physiol*. 2017;595:2839-2847.
85. Dzeja PP, Bortolon R, Perez-Terzic C, Holmuhamedov EL, Terzic A. Energetic communication between mitochondria and nucleus directed by catalyzed phosphotransfer. *Proc Natl Acad Sci USA*. 2002;99:10156-10161.

86. Prachar J. Intimate contacts of mitochondria with nuclear envelope as a potential energy gateway for nucleo-cytoplasmic mRNA transport. *Gen Physiol Biophys*. 2003;22:525-534.
87. Desai R, East DA, Hardy L, et al. Mitochondria form contact sites with the nucleus to couple prosurvival retrograde response. *Sci Adv*. 2020;6:eabc9955.

SUPPORTING INFORMATION

Additional supporting information can be found online in the Supporting Information section at the end of this article.

How to cite this article: Mahadev Bhat S, Sieck GC. Heterogeneous distribution of mitochondria and succinate dehydrogenase activity in human airway smooth muscle cells. *FASEB BioAdvances*. 2024;6:159-176. doi:10.1096/fba.2024-00047